



HAL
open science

Theoretical study of the arc motion in the hollow cathode of a dc thermal plasma torch

Francis Sambou, Jean Jacques Gonzalez, M Benmouffok, Pierre Freton

► **To cite this version:**

Francis Sambou, Jean Jacques Gonzalez, M Benmouffok, Pierre Freton. Theoretical study of the arc motion in the hollow cathode of a dc thermal plasma torch. *Journal of Physics D: Applied Physics*, 2021, 55 (2), pp.025201. 10.1088/1361-6463/ac2a76 . hal-03753408v2

HAL Id: hal-03753408

<https://hal.science/hal-03753408v2>

Submitted on 18 Aug 2022

HAL is a multi-disciplinary open access archive for the deposit and dissemination of scientific research documents, whether they are published or not. The documents may come from teaching and research institutions in France or abroad, or from public or private research centers.

L'archive ouverte pluridisciplinaire **HAL**, est destinée au dépôt et à la diffusion de documents scientifiques de niveau recherche, publiés ou non, émanant des établissements d'enseignement et de recherche français ou étrangers, des laboratoires publics ou privés.

Theoretical study of the arc motion in the hollow cathode of a dc thermal plasma torch

F Sambou, J J Gonzalez, M Benmouffok and P Freton

LAPLACE, Université de Toulouse, INPT, CNRS, UPS, 118 route de Narbonne, F-31062
Toulouse, France

E-mail: pierre.freton@laplace.univ-tlse.fr

Abstract

A 3D model of a hollow cathode of a thermal plasma torch was developed to study the motion of the electric arc in the upstream part as well as its influence on the characteristics of the thermal plasma generated at the entrance of the downstream part (anode). The translational motion along the axis and the rotational velocity of the cathodic arc root are studied. The results of the model are presented and compared with those of the literature and also with experimental results. Good agreements on the prediction of the axial arc position and of the rotational speed of the arc root are found with the literature. A correlation is also shown between the theoretical positions of the arc root and the experimental traces of erosion observed on the cathode.

Keywords: hollow cathode, arc motion, 3D model

1. Introduction

Thermal plasma torches with hollow cathode are used in several industrial applications such as: waste treatment, production of reducing gases in the steel industry, petro chemistry [1-3]. This plasma torch technology is used for high power outputs in the MW range [4] and allows the generation of large volumes of thermal plasma at very high enthalpies in the range 107-108J/kg and temperatures between 3000K and 15000K [1]. These torches have some specificities that make their study delicate: (1) a hollow cathode, (2) a vortex gas injection between the electrodes, (3) an external magnetic field in order to rotate the arc root in the upstream electrode and to limit its erosion. The complexity of their geometry and the extreme conditions prevailing in these torches (High Power) make their experimental studies difficult and expensive [4]. The experimental characterizations of hollow torch technologies are devoted to measurements of macroscopic physical quantities such as: arc voltage, emitted sound waves, and temperature and velocity fields of the jet at the torch exit. It does not allow a detailed understanding of their internal functioning as the flow path from the injection chamber or description of the arc attachment in the hollow cathode. In the anode region, the difficulty to visualize the arc anode root or to quantify the erosion is also difficult, however studies performed not in hollow cathode but in rod cathode have been published showing new interesting results and possibilities [5, 6]. Because of these limitations in hollow cathode, numerical studies are the most suitable for a better understanding of their internal behavior.

In the literature, few studies on this torch technology exist probably due to the complexity of their configuration. In the 1990s, Brillhac et al [4] carried out a theoretical and experimental study of a thermal plasma torch with a hollow cathode for a power less than 100 kW and without an external magnetic field. During their experimental study, they noted the positioning of the wear zones as a function of the operating conditions and linked the position of this zone to the variations of the axial component of the velocity in close proximity to the cathode surface (0.5mm from the surface) using a cold theoretical analysis of the plasma gas flow (in the absence of electric arc) using the numerical code "MELODIE". Thanks to their experimental electrical and acoustic measurements, they qualitatively stipulate that the variations in the output characteristics of the torch are related to the fluctuations of the arc within the cathode. In the 2000s, again through the experiment, Hur et al [7-8] studied the behavior of a 200kW thermal plasma torch in the absence of an external magnetic field. Based on the same principle as Brillhac

et al [4] concerning the analysis of the cold plasma gas flow and thanks to their experimental measurements they also correlated the position of the wear zone to the variations of the axial component of the cold plasma gas flow velocity near the cathode. This qualitative technique for determining the position of the wear zone on the surface of the cathode by Brillhac et al [4] is also used in configurations in the presence of a magnetic field by Park et al [9]. In their study, they consider the external magnetic field to be axial and constant. In the 1990s Minoo et al [10] conducted an experimental and theoretical study on this type of torch technology and showed that the positioning of the arc root on the cathode surface (position of the wear zone) results from an equilibrium between the magnetic and drag forces of the arc root by the flowing plasma gas. Another study in 2009 by Freton et al [11] shows that the external magnetic field, in particular its radial component, has a strong influence on the axial position of the arc root on the cathode surface. They find through their results that the external magnetic field is far from constant and that the arc root tends to reach a position where the radial component of the external magnetic field is at its maximum.

In this paper, we present a 3D numerical model that we have developed to represent the motion of the arc and its influence on the thermal plasma characteristics. We focus the study only on the upstream part of the torch (cathode). The first part of this paper will be devoted to the presentation of the numerical model. In the second part, a particular attention will be devoted to the calculation of the magnetic field generated by the external coil. The third part will present and discuss the results of the model for given operating conditions with a comparison with the literature. Finally, in the last part, a conclusion will be given.

2. Numerical model

In the framework of this study, the numerical tool used to solve the equations is the commercial code Ansys Fluent, which is widely used in the literature for the study of fluid flows at low temperatures, by solving the Navier-Stokes equations of fluid mechanics. This software has functionalities allowing the user to add additional terms to the Navier-Stokes equations (source terms) as well as additional equations. These functionalities, called UDF (User Define Function), are external functions that the user will be able to define and implement in the software to adapt it to his problematic. Thus in the framework of our study, these functions are used for the description of plasmas properties, specific source terms and for the electromagnetic aspect of thermal plasmas. To solve the equations, this tool uses the finite volume method proposed by Patankar et al [12]. According to this method, the equations are rewritten in the form of the generalized differential equation (1):

$$\frac{\partial(\rho\phi)}{\partial t} + \text{div}(\rho\vec{v}\phi) = \text{div}\left(\Gamma_{\phi}\cdot\overrightarrow{\text{grad}}(\phi)\right) + S_{\phi} \quad (1)$$

In this equation, we have respectively the temporal term, the convective term, the diffusive term and the source term (S_{ϕ}). ϕ is the physical property studied, Γ_{ϕ} its diffusion coefficient, ρ the mass density, and \vec{v} the velocity.

2.1. Hypothesis and equations

2.1.1. Hypothesis. We use air as plasma gas. We consider that the thermal plasma created is a Newtonian fluid in laminar flow, at local thermodynamic equilibrium (LTE). The LTE hypothesis is used for the calculation of the properties of the thermal air plasma [13] such as thermodynamics, transport and radiative properties. This assumption is classically adopted in the plasma core, nevertheless departures from equilibrium can exist in plasma surrounding and in the electrodes sheathes. According to P. Andre et al [X], for heavy species temperature $T=10\text{kK}$, the frequency collision of the electron with other particles is at equilibrium equals to 10^{13} s^{-1} and equals to $5\cdot 10^{13}\text{ s}^{-1}$ for $\theta=Te/Th=3$ (ratio of electronic temperature on heavy one). This number of collisions by second is important compared to the calculation time classically used in the simulation ($10\mu\text{s}$ in our case) allowing considering LTE assumption. For validating the laminar flow hypothesis, we use the method suggested by Sinkevich et al [14] for thermal plasma to estimate the Reynolds number. Indeed, in the case of thermal plasma, the transport and thermal proprieties change highlight with the plasma flow dimensional characteristics (essentially in the radius direction for a tubular channel). This highlight change makes difficulty to choose the characteristics of the plasma flow allowing the Reynolds number estimation. Therefore, this method suggests estimating the Reynolds number by calculating mean values of the characteristics of the plasma flow. According to this method, we obtain a Reynolds numbers within the torch below 500. That allows us to consider a laminar flow hypothesis in our study. The radiation source term is taken into account as a loss term in the energy equation by the net emission coefficient method [15]. The walls erosion due to the arc attachment or incoming radiation from the arc is not taken into account.

2.1.2. Equations. The equations solved with the source terms are as follows:

- The mass conservation equation :

$$\frac{\partial \rho}{\partial t} + \vec{\nabla} \cdot (\rho \vec{v}) = 0 \quad (2)$$

Where t represents the time, $\vec{\nabla}$ is the spatial gradient operator, ρ is the mass density, and \vec{v} is the vector velocity

- The momentum conservation equation:

$$\frac{\partial(\rho \vec{v})}{\partial t} + \vec{\nabla} \cdot (\rho \vec{v} \vec{v}) = \vec{\nabla}(\mu \vec{\nabla} \cdot \vec{v}) + S_v \quad (3)$$

$$\text{Where } S_v = -\vec{\nabla}(P) + \vec{\nabla} \cdot \bar{\tau} + \vec{j} \times \vec{B} + \rho \vec{g} \quad (4)$$

S_v is the momentum source term where we distinguish respectively pressure forces (P), viscous stresses $\bar{\tau}$, Lorentz forces (product of the current density by the magnetic field $\vec{j} \times \vec{B}$) and gravity \vec{g} . μ being the viscosity. The stress tensor $\bar{\tau}$ is given for a Newtonian fluid by the relation:

$$\tau_{ij} = \mu \left[\left(\frac{\partial v_i}{\partial j} + \frac{\partial v_j}{\partial i} \right) - \frac{2}{3} \frac{\partial v_i}{\partial i} \delta_{ij} \right] \quad (5)$$

Where the index i and j correspond to the different components of the coordinate system, v_i and v_j are the velocity components. The symbol $\delta_{ij} = 1$ if $i=j$ and $\delta_{ij} = 0$ elsewhere

- The energy conservation equation:

$$\frac{\partial(\rho h)}{\partial t} + \vec{\nabla} \cdot (\rho \vec{v} h) = \vec{\nabla} \cdot \left(\frac{K}{C_p} \vec{\nabla} h \right) + S_H \quad (6)$$

$$\text{Where } S_H = \frac{\vec{j}^2}{\sigma} - U + \frac{5}{2} \frac{k_B}{e} \vec{j} \cdot \vec{\nabla} \left(\frac{T}{C_p} \right) \quad (7)$$

S_H is the energy source term, where we have respectively the joule effect (Ratio of the square of current density on the electrical conductivity σ), radiative losses (U), and enthalpic flux of the electrons. k_B is the Boltzmann constant, C_p the specific heat at constant pressure, K the thermal conductivity, h the enthalpy, T the temperature and e the elementary charge.

According to the net emission coefficient method, the radiative losses are given by:

$$U = 4\pi \varepsilon_N \quad (8)$$

Where ε_N represents the net emission coefficient. For the description of the electromagnetic phenomena of the plasma, it is necessary, in addition to the fluid equations, to solve the equation of the electric potential and the vector potential equations. These equations allow the calculation of electric and magnetic fields respectively. These electromagnetic fields act on the charge carriers of the plasma (electrons and ions) and consequently lead to the coupling between the fluid and electromagnetic equations by acting as sources (through the Lorentz force) in the momentum equation (3) and energy (joule effect) in the energy equation (6). The electromagnetic equations are established by assuming that the plasma medium is a succession of stationary states.

In order to satisfy the current continuity equation, we use the equation (9) where V designates the scalar potential.

$$\vec{\nabla} \cdot (\sigma \vec{\nabla} V) = 0 \quad (9)$$

Equation (9) is used to calculate the electric field (10) and the current density (11):

$$\vec{E} = -\vec{\nabla} V \quad (10)$$

$$\vec{j} = \sigma \vec{E} \quad (11)$$

For the calculation of the magnetic field \vec{B} , two methods are generally used in the literature [16]:

- Solving the potential vector equation \vec{A} using the Laplacian $\Delta\vec{A}$:

$$\Delta\vec{A} = -\mu_0\vec{j} \quad (12)$$

μ_0 is the magnetic permeability of vacuum

- Biot & Savart law :

$$\vec{A}(\vec{r}) = \frac{\mu_0}{4\pi} \iiint \frac{\vec{j}(\vec{r}')}{|\vec{r}-\vec{r}'|} d\vec{r}'^3 \quad (13)$$

Where \vec{r} is the position of the point where we want to calculate the magnetic field and \vec{r}' is the position of the current element contributing to this magnetic field. The magnetic field is deduced by the vector potential according to the relation (14):

$$\vec{B} = \vec{\nabla} \times \vec{A} \quad (14)$$

In this study, we use a Cartesian coordinate system. The set of conservations equations solved by the model are the same equations described by Freton et al [11].

2.2. Geometry

In the figure 1, we present the cathode geometry of the studied torch.

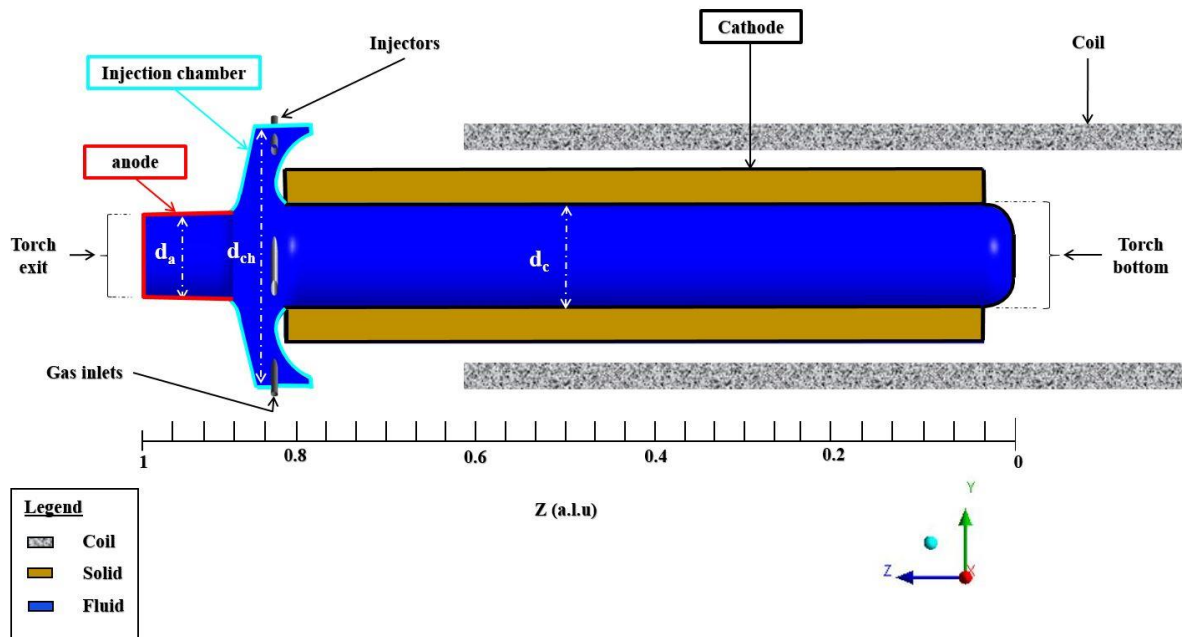


Figure 1 – Overview of the studied device including the simplified scheme and position of the coil

The torch is made up of two electrodes (anode and cathode) and an injection chamber composed by 6 injectors inclined at an angle of 20° through which the plasma gas is injected. The anode and the cathode are electrically isolated by insulators in the injection chamber. This configuration of the injectors makes it possible to produce a vortex-type flow of the plasma gas. The torch is also equipped with an external coil in the cathode side. The internal details of the torch constrain the plasma formation, nevertheless the external magnetic field produced by the coil and the localization of its maximum value depending on the coil position act on the arc root rotation and stabilization. The management of the downstream arc over the anode can also in some configurations be important

but in our studied configuration it doesn't exist in the anode side external magnetic field produced by a coil. The cathode's coil is represented in the Figure 1. Note that for the geometry studied, the anode part has been truncated just after the injection chamber in order to focus the study of the arc motion only in the cathode. Gris parts represent the coil, and the torch bottom is located in the right side. In this study, the torch dimensions are expressed in dimensional length unit (a.l.u) as preconized by our industrial partner and for confidentiality reasons. However the geometry is drawn as per scale maintaining the aspect ratio. The total length of the geometry presented in Figure 1 is about 30cm. The inlet diameters of the hollow cathode and of the anode are respectively $d_c=0.1$ a.l.u., $d_a= 0.083$ a.l.u and $d_{ch}= 0.26$ a.l.u (Figure 1).

2.2.1. Boundary conditions. Table 1 presents the boundary conditions.

Table 1. Boundary conditions

Boundary	Injectors inlet	Torch exit	Walls
T[K]	300	$\vec{\nabla}T \cdot \vec{n} = 0$	300
D [g.s⁻¹]	37	-	-
P [atm]	-	$\vec{\nabla}P \cdot \vec{n} = 0$	$\vec{\nabla}P \cdot \vec{n} = 0$
V [V]	$\vec{\nabla}V \cdot \vec{n} = 0$	0	$\vec{\nabla}V \cdot \vec{n} = 0$
$v_{i=x,y,z}$[m/s]	$\vec{\nabla}v_i \cdot \vec{n} = 0$	$\vec{\nabla}v_i \cdot \vec{n} = 0$	$\vec{\nabla}v_i \cdot \vec{n} = 0$
$A_{i=x,y,z}$[T.m]	$\vec{\nabla}A_i \cdot \vec{n} = 0$	$\vec{\nabla}A_i \cdot \vec{n} = 0$	$\vec{\nabla}A_i \cdot \vec{n} = 0$

In Table 1, D is the inlet mass flow rate and $v_{i=x,y,z}$ and $A_{i=x,y,z}$ the three components respectively of the velocity and vector potential.

The current, after passing in the external coil, flows through the torch in the solid part. Depending on the plasma conditions in the fluid part, the current path is self-determined. We therefore apply an arbitrary current density boundary condition in the solid part of the cathode (\vec{j}_{crown}) on a crown located below the bottom of the cathode (figure 2).

On the downstream section (Torch exit, Figure 1) of the anode portion, we consider a porous anode condition [11] that is to say a zero electric potential boundary condition where the arc column will hang (Figure 2). In order to take into account the contribution of the magnetic field due to the current flow in the torch frame, Biot and Savart's law (equation 13) was used as a closing boundary condition on the solid boundaries for the calculation of the vector potential. In the solid, we solve only the scalar potential. In the Figure 2, we present a general view of the mesh.

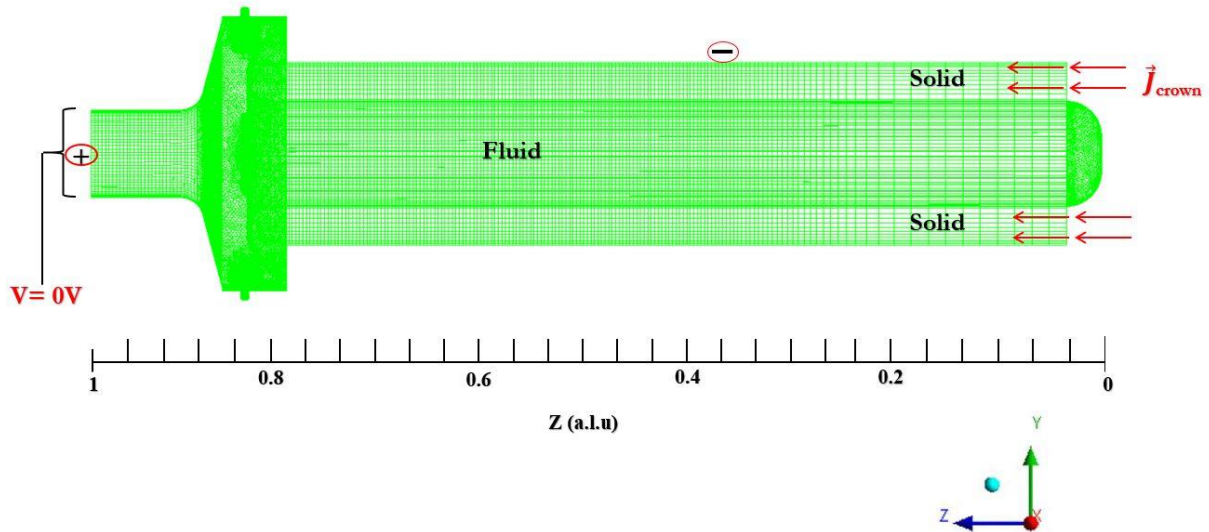


Figure 2 – Domains studied (Solid and Fluid) and grid

The mesh has been refined at the electrodes surfaces (boundary between fluid and solid parts) as well as at the injectors region in order to correctly capture the physical phenomena in these areas. To take into account the current flow in the cathode, the solid part of the cathode is also meshed. After a specific study on the mesh to obtain an invariant solution on converged results, the total resulting mesh has about 670 000 cells with a volume range from $6.3 \cdot 10^{-2} \text{mm}^3$ to $3.4 \cdot 10^{-1} \text{mm}^3$. The larger cells are located at the top of the hollow cathode far from the arc presence as the smaller cells are in the plasma core on the walls where the arc root is attached. It can be seen in Figure 2 that the mesh is refined in the plasma area where will be located the plasma. It consists of two types of mesh: (1) an un-structured mesh: in the injection chamber and at the cathode extremity; (2) a structured mesh: in the electrodes as well as in the inter-electrode space.

2.2.2. Procedure for initializing the calculation. In order to allow the flow of electric current in the plasma gas between the two electrodes for arcing, a hot conductive channel must be defined. This is done by introducing one energy source term via a UDF. The conductive channel was ignited between the axial positions $z=0.67$ a.u.l. and $z=1$ a.u.l. from the bottom of the cathode localized at $z=0$ a.u.l., taken as the origin of the space in the model. The volume of conducting channel is approximately $3.17 \cdot 10^{-6} \text{m}^3$ and the instantaneous power deposited in the initial channel is around 125kW. This channel corresponds to an arc length and to one diameter equal respectively to 0.1m and $6 \cdot 10^{-3} \text{m}$. The power is introduced as source term in the energy equation in all the cells volumes of the channel leading in our case to a mean initial temperature around 10kK. The initial temperature needs to be enough to allow a conducting channel. Regarding to the electrical conductivity variation versus temperature values from 9kK can be chosen. Higher values can be considered but the deposited energy must be negligible compared to the injected power in order to not introduce energy which could be longer to dissipate. Then the fluid and electromagnetic equations described above for the thermal plasma part are solved for 5 time steps ($5 \times 10 \mu\text{s}$) corresponding to a total deposited energy around 6.25J. Once the conductor channel has been established, we then run the whole calculation. The conductive channel obtained after the arcing is the one shown in Figure 3 and materialized by the 7kK temperature iso-surface. The temperature is in the range 7kK to 11kK. Of course the value of the deposited energy doesn't affect the results as after the channel establishment the power in the plasma is calculated by the imposed value of the current intensity and the resulting drop voltage directly calculated by the scalar potential resolution.

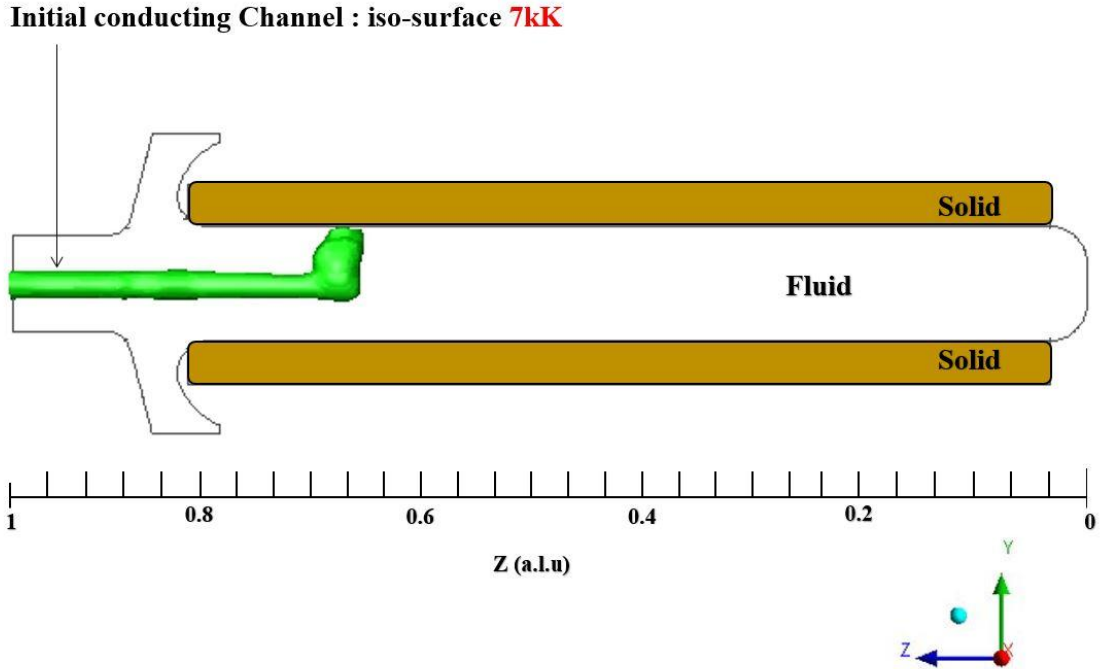


Figure 3 – Initial conductor channel in the simulation

2.3. Arc attachment movements

In order to determine the position where the arc root is attached to the cathode surface, we consider the model proposed by Lindmayer et al [17] developed in the framework of the study of arc displacement in low voltage circuit breakers [18-24]. This model is based on a calculation of the effective electrical conductivity at each point on the surface [17,25,26] and allows introducing an additional sheath voltage drop the point of attachment having the highest conductivity. The rigorous numerical treatment of these zones would require the implementation of non-thermal equilibrium models that are more expensive in computing time [27] [28].

Once this threshold voltage has been reached and the arc has established itself between the electrodes, the voltage drop in these zones becomes independent of the increase in current density [17] and tends towards a constant voltage depending on the electrode material (10 Volt for copper). Thus, a thin layer of thickness Δr is defined near the surface of the cathode. On this layer, a local value of the effective electrical conductivity σ_{eff} is calculated according to one of the voltage-current density characteristics [25] and the relation (15):

$$\sigma_{eff}(J) = J \cdot \frac{\Delta r}{V_s(J)} \quad (15)$$

The study of the motion of the arc by this model requires modeling the current path in the electrode, which imposes to mesh the electrode framework (solid part).

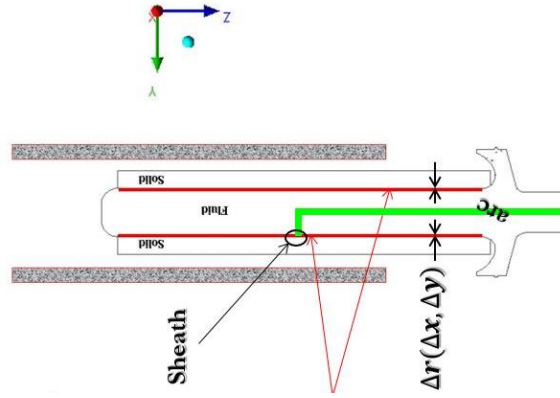


Figure 4 – The layer defined for the Lindmayer model [17]

The Figure 4 shows a schematic representation of the arc with the positions of the sheath. In [25] four curves (a, b, c and d) whose variations are dependent on the arc initiation threshold voltage (23.3V, 19.7V, 17.1V and 10V) can be used. The highest is the voltage peak; the most difficult is the motion of the arc. For the instantaneous displacement of the cathodic arc root, one considers at each instant through the model, the position of the arc root as corresponding to the weighted barycenter of each point of the cathode surface by its electrical conductivity, according to relations (16) and (17) respectively for the instantaneous axial and azimuthal positions :

$$Z_{cat}(t) = \frac{\sum_{i=1}^{n_p} \sigma_i(t) \cdot Z_i(t)}{\sum_{i=1}^{n_p} \sigma_i(t)} \quad (16)$$

$$\theta(t) = \frac{\sum_{i=1}^{n_p} \sigma_i(t) \cdot \theta_i(t)}{\sum_{i=1}^{n_p} \sigma_i(t)} \quad (17)$$

Where :

- $\sigma_i(t)$ represents the electrical conductivity of point i of the cathode surface;
- $Z_i(t)$ and $\theta_i(t)$ are respectively the axial and azimuthal positions of point i on the cathode surface ;
- n_p is the total number of points on the cathode surface.

2.4. Calculation of the magnetic field generated by the coil

The external coil of this torch is a 3-layer solenoid type, each of the 3 layers having a different number of turns. To determine the distribution of the magnetic field generated by the coil we used an analytical method from the literature proposed by Conway [29] adapted to our coil configuration. This method determines the magnetic field generated by a simple coil of finite dimension using elliptic integrals by integrating the Maxwell's equations of magneto statics, (18) and (19).

$$\vec{\nabla} \times \vec{B} = \mu_0 \vec{J} \quad (18)$$

$$\vec{\nabla} \cdot \vec{B} = 0 \quad (19)$$

\vec{B} represents the magnetic field, \vec{J} the current density, and μ_0 the vacuum permittivity. By introducing relation (14) in equation (19), we obtain the equation:

$$\vec{\nabla} \cdot \vec{A} = 0 \quad (20)$$

By introducing relation (14) into equation (18) and using equation (20), the vector potential satisfies to the potential vector equation (12). In the case of an axisymmetric solenoid in cylindrical coordinates, only the azimuthal components of the vector potential (A_θ) and current density (J_θ) contribute to the generated magnetic field. Thus, equation (12) can be rewritten in the azimuthal direction by equation (21):

$$\nabla^2(A_\theta(r, z)) = -\mu_0 J_\theta(r, z) \quad (21)$$

The relation (14) allows expressing the axial and radial components of the magnetic field as a function of the azimuthal component of the vector potential in cylindrical coordinates system (22) and (23):

$$B_z(r, z) = \frac{1}{r} \frac{\partial}{\partial r} (r A_\theta(r, z)) \quad (22)$$

$$B_r(r, z) = -\frac{\partial A_\theta(r, z)}{\partial z} \quad (23)$$

Note that there can be no toroidal component i.e. $B_\theta(r, z) = 0$. By integrating equation (21) over the entire current distribution using elliptic integrals, Conway obtains the following analytical relationships for the axial and radial components of the magnetic field for a simple solenoid of finite dimension. These analytical relationships can be written by introducing the number of turns N of the solenoid by [11]:

$$B_r(r, z) = \frac{\mu_0 N I}{2} (I_{(0,1,1)}(R, r, |Z_2 - z|) - I_{(0,1,1)}(R, r, |Z_1 - z|)) \quad (24)$$

$$B_z(r, z) = \frac{\mu_0 N I}{2} (I_{(0,1,0)}(R, r, |Z_1 - z|) - I_{(0,1,0)}(R, r, |Z_2 - z|)) \quad \text{if } (z < Z_1) \quad (25)$$

$$B_z(r, z) = \frac{\mu_0 N I}{2} (2I_{(0,1,0)}(R, r, 0) - I_{(0,1,0)}(R, r, |Z_1 - z|) - I_{(0,1,0)}(R, r, |Z_2 - z|)) \quad \text{if } (Z_1 < z < Z_2) \quad (26)$$

$$B_z(r, z) = \frac{\mu_0 N I}{2} (I_{(0,1,0)}(R, r, |Z_2 - z|) - I_{(0,1,0)}(R, r, |Z_1 - z|)) \quad \text{if } (z > Z_2) \quad (27)$$

I is the intensity of the current in the solenoid, R its radius, Z_1 and Z_2 the positions of its extremities. The functions $I_{(0,1,1)}$ and $I_{(0,1,0)}$ are the elliptic integrals or Bessel-Laplace's integrals [29-30].

3. Results

For this study, we applied an arc current intensity of 260A for an air flow rate imposed on the injectors of 37g/sec. The curve (c) [25] is used to consider the arc motion on a copper surface.

3.1. Magnetic field

In this section, we present the distribution of the components of the external magnetic field generated by the coil, calculated using the analytical relationships proposed by Conway et al [29] adapted to our coil configuration.

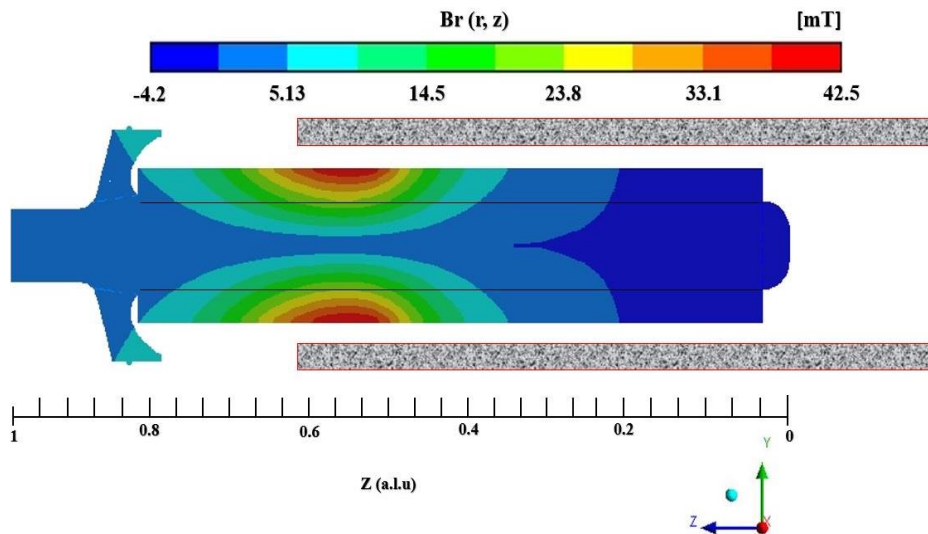


Figure 5 – Field of the radial component of the magnetic field

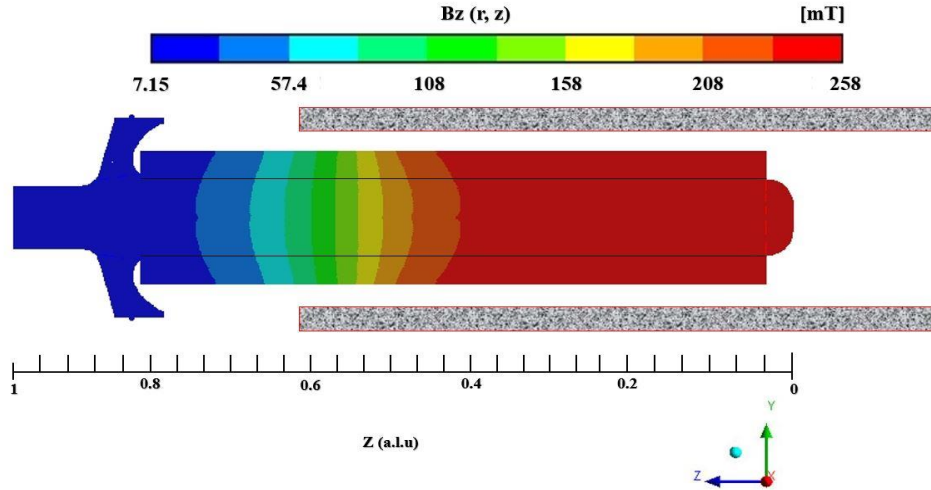


Figure 6 – Field of the axial component of the magnetic field

Figures 5 and 6 show respectively the distributions of the radial and axial components of the magnetic field. The radial and axial magnetic field components have axisymmetric distributions. The maximum values of the radial and axial components of the magnetic field created by the coil are $B_{r_{\max}}= 25\text{mT}$ and $B_{z_{\max}}=250\text{mT}$, respectively. The black lines represent the position of the inner diameter of the cathode where the fluid flows.

For this study, the axial component of the magnetic field responsible for the rotational motion of the arc is applied in such a way that it causes the cathodic arc root to rotate in the opposite direction of the vortex injecting plasma gas. Since the motion of the arc root is induced by the application of an external magnetic field, it is obvious that a reversal of the direction of the magnetic field should be able to impart a motion of the arc root just in the reverse direction [5]. Note that the total magnetic field within the torch represents the contributions of the magnetic field generated by the coil as well as the magnetic fields generated by the arc current and the cathode current.

3.2. Arc behaviour in the hollow cathode

In the Figure 7, we present the temporal behavior of the electric arc within the geometry studied, which is represented by the iso-surface 7kK . The sinuous plasma behavior part due to the external magnetic field, vortex injection, and changes of the arc root position is related to the hollow cathode (above red line) as the cylindrical part (bellow red line) is related to the portion of the anode part. This behavior of the electric arc is the consequence of the interactions between the blowing of the vortex airflow and its rotation under the action of the magnetic field.

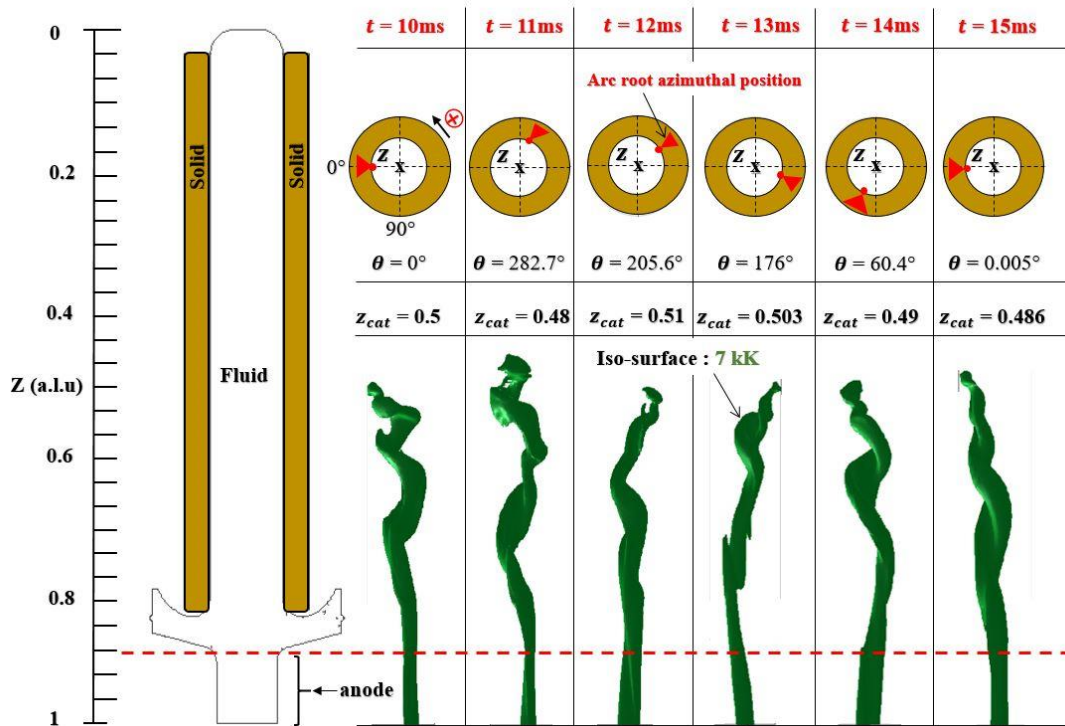


Figure 7 – Arc behavior within the geometry

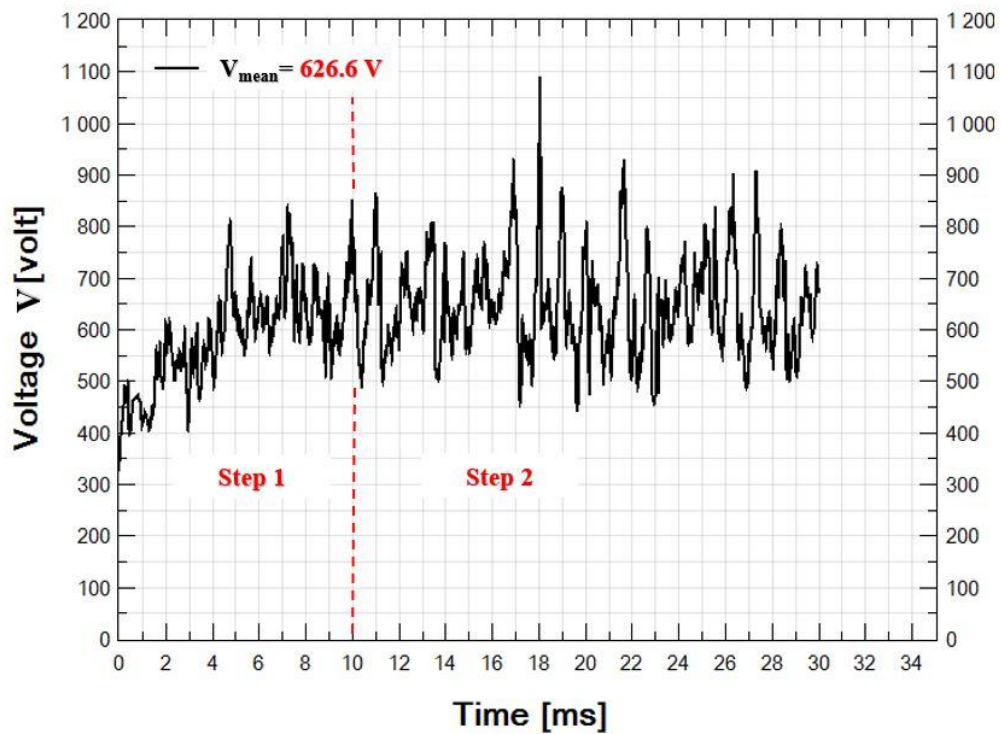


Figure 8 – Electric arc voltage versus time

These non-linear evolutions of the arc configuration can also be distinguished in terms of the evolution of its voltage with time, represented in the Figure 8, evolving around an average value, $V_{\text{mean}} = 626\text{V}$. Two parts can be distinguished in the voltage evolution: (Step 1) the arc under the influence of convective and magnetic forces is pushed in direction of the top of the cathode and simultaneously begins to rotate. Progressively the convective

force diminishes and an axial equilibrium position exists after 10ms with a mean voltage value around $V_{\text{mean}} = 626\text{V}$, (Step 2) then the arc slowly oscillates from this axial position and still rotates due to the magnetic field. The rotational velocity keeps roughly the same, nevertheless the arc length has increased and the arc column submitted to convective and magnetic forces is more constraint leading to distortions and length variations illustrated by the amplitude of the voltage variations.

3.3. Cathodic arc root motion

In the Figure 9, we have represented on the left side the evolution of the axial position of the arc root on the cathode surface as a function of time and on the right side the axial profiles of the radial and axial components of the magnetic field generated by the coil. The position of the arc root at time $t=0\text{ms}$ corresponds to its initialization position ($z=0.67$ a.l.u). The radial component of the external magnetic field being order smaller than the axial component, we had multiplied it by 10 in order to clearly see its spatial profile.

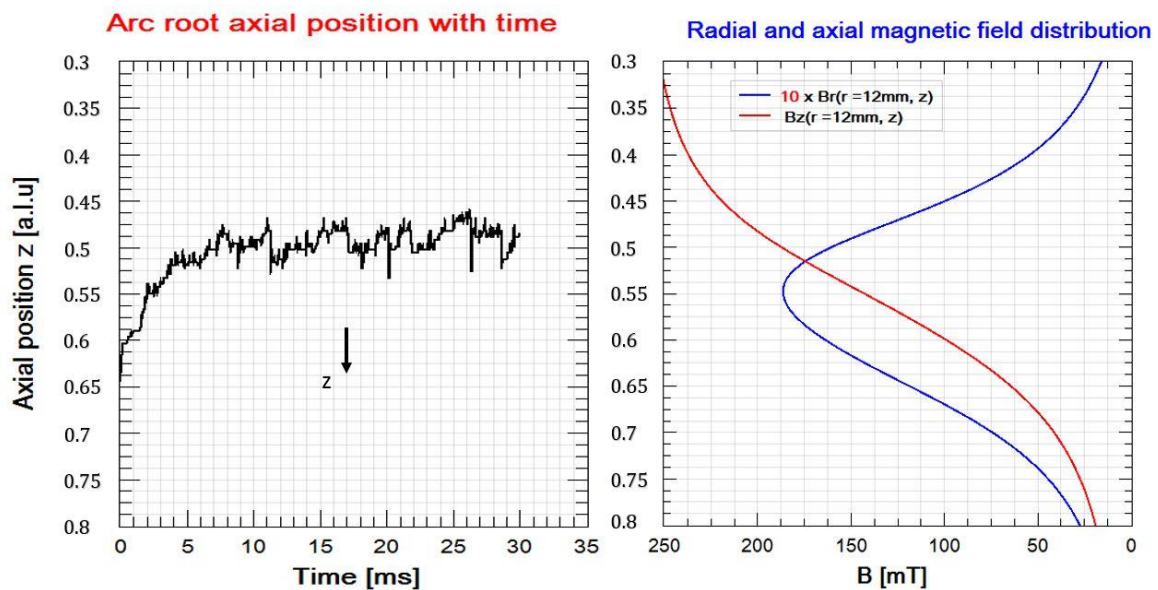


Figure 9 – Arc root axial position versus time in the left and, in the right radial (in blue) and axial (in red) external magnetic field components. $I=260\text{A}$, $D=0.037\text{kg/s}$.

This figure shows the instantaneous arc root axial position estimated by the equation 16. The arc root moves in a non-linear way towards the bottom of the cathode up to a mean equilibrium area where it oscillates. In this figure, the arc rotation equilibrium zone is delimited by the axial positions $z=0.47$ and 0.53 a.l.u. This non-linear axial movement of the arc root is the consequence of the arc fluctuations due to the joint actions of the plasma gas flow and the external magnetic field. The Figure 9 show also that the axial root attachment converges to a position located close to the maximum of the radial component of the magnetic field. Freton et al [11] have also observed a correlation between the rotational equilibrium area of the arc root with the position of the maximum values of the radial component of the external magnetic field.

In order to study whether there was a correlation between the erosion zones and the position of the rotational equilibrium zone, our industrial partner Europlasma carried out thickness measurements using an ultrasonic thickness gauge (from Krautkramer Branson). The measuring principle is as follows: Ultrasonic pulses are transmitted to the electrode material by a probe in contact with the surface of the cathode material. Some of the pulses are reflected at the surface in contact with the material while others pass through the material to its opposite side where they are reflected. By analyzing the paths taken by the sound pulses reflected at the contact surface of the probe with the material and those reflected at the opposite surface of the contact area, the thickness of the area of the material through which the ultrasonic pulses pass can be deduced. The electrode erosion is a slow process and the thickness of the eroded area changes versus time. This eroded area is so most visible after several hours of running. Nevertheless the eroded area position keeps the same. The accuracy in thickness measurements given in the technical documentation is about 0.25mm . In the figure 10, we have represented the axial position of the

rotation equilibrium zone predicted by the model, which we have compared to the experimental eroded zone obtained after several hours of running.

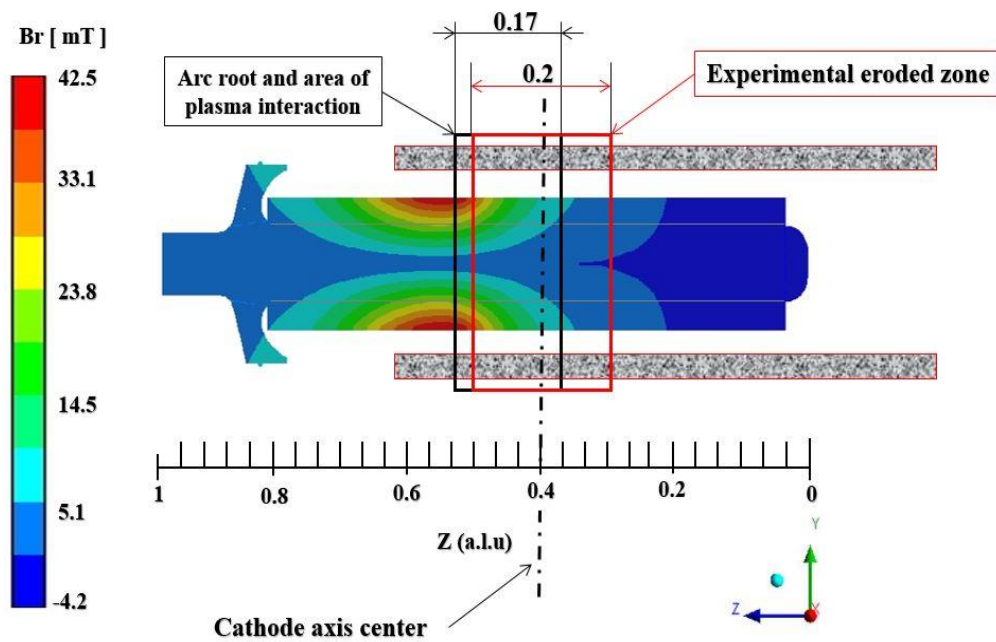


Figure 10 – Wear position: experiment and model

Figure 10 shows an overlap of the two zones: the theoretical hanging zone (arc root attachment: black frame 0.17 a.l.u. wide) and the experimentally observed one (wear zone: red frame 0.2 a.l.u. wide). Due to convective effects, the mean axial root position (Figure 9) is not located in the middle of the area of plasma interaction with the wall (Figure 10) as the plasma is blown by the upstream flow.

The arc interaction on the electrode leads to a heat transfer. Several physical quantities act as the radiation, the conduction and the electric components due to the current path between plasma and material. Depending on the arc motion and to the cooling system the wall temperature is more or less dissipated leading to erosion. In our model the sheath is not described and an “artificial method” is used to represent the sheath resistivity. Depending on voltage gradient [25] and on the curve chosen, more or less current is allowed to circulate through a calculated value of the electrical conductivity. The choice of the curve (a-b-c-d) could also allowed to adjust if necessary the dimension of the eroded zone. In case of departure from experimental results, the value of the ignition voltage has to be chosen on the basis of the measurement results [31]. The higher is the ignition voltage, the smaller is the eroded area and the later begins the new arc root position. Nevertheless one can see in the figure 10 that our theoretical results on the prediction of the eroded zone show a similarity with the eroded zone found experimentally applying curve c.

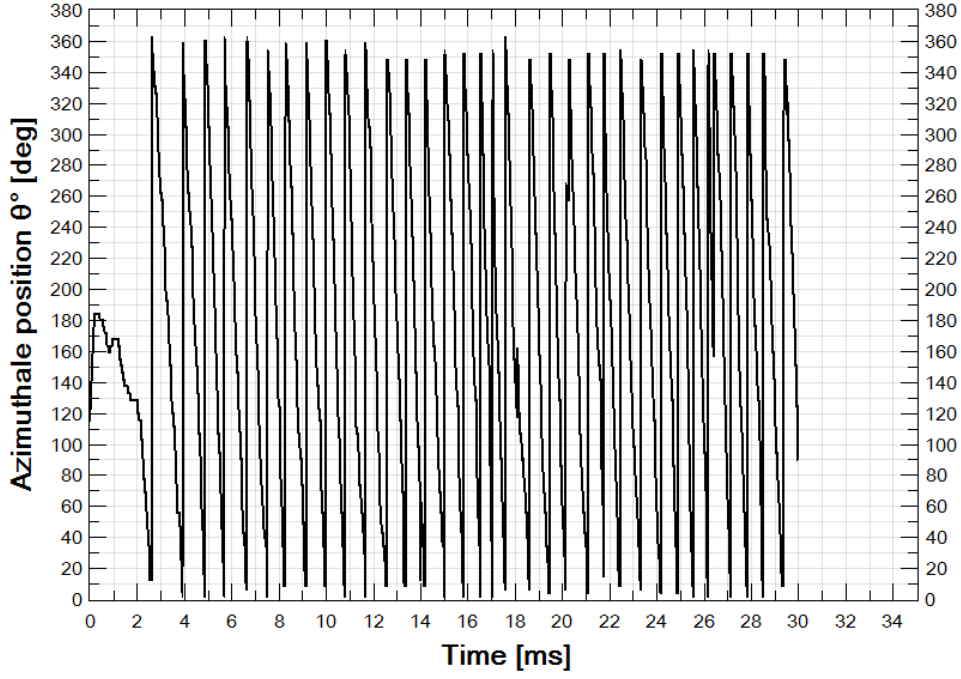


Figure 11 – Arc root azimuthal position versus time

Figure 11 shows the azimuthal position of the arc root as a function of time estimated by equation 17. The figure shows a quasi-periodic azimuthal revolution of the arc around the axis of the torch. If the attachment is constricted there is a formation of arc root on the nozzle and the external magnetic field imparts a rotational movement to the constricted attachment due to appreciable Lorentz forces. This arc root movement is sometimes designed, induced root movement (IRM) [5]. Due to the forces the arc root rotates, each turn corresponds to one maximum in the Figure 11. The arc root pulls the plasma column which has a tortuous behavior leading sometime to new arc root position in back side and irregularities or disturbances on the arc root evolution versus time as observed at time $t=18\text{ms}$. In order to estimate the frequencies and speeds of rotation of the arc root and to compare them with the literature, we proceed as follows:

Knowing the number of revolutions $N(t)$ carried out by the arc root, given by the relation (28), we estimate instantaneous frequencies and rotational speeds of the arc root according to relations (29) and (30) respectively.

$$N(t) = \frac{\sum |\theta(t+\Delta t) - \theta(t)|}{2\pi} \quad (28)$$

Where:

- $\theta(t)$: represents the azimuthal position of the arc root at time t .
- $\theta(t + \Delta t)$: represents the azimuthal position of the arc root at time $t + \Delta t$
- $\Delta t = 10^{-5}$ s: is the calculation time step.

$$f(t) = \frac{N(t)}{n_t \Delta t} \quad (29)$$

Where: n_t represents the number of time step Δt associated to $N(t)$.

$$v_{arc}(t) = \pi d_c f(t) \quad (30)$$

d_c is the internal cathode diameter. In the Figure 12, we present the frequency variations (left side) and the rotational arc root velocity versus time (right side), estimated respectively by relation (29) and (30). This figure shows that the frequency and the speed rotation of the arc increases rapidly from the first moments and then tends towards constant values of 1.14 kHz and $107\text{m}\cdot\text{s}^{-1}$ respectively.

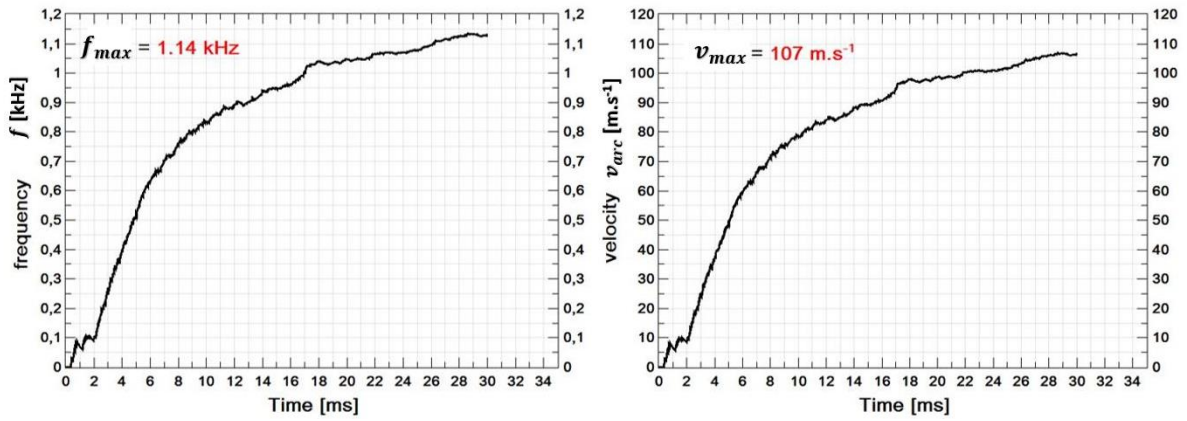


Figure 12 – Arc frequency and velocity versus time

Essiptchouk et al [32] carried out an experimental study on the rotational speed of the electric arc within this torch technology. In their experiment, they deduce a rotational speed of the electric arc given by:

$$v_{arc} = 78 \cdot I^{4/9} B^{0.6} \rho_0^{-8/9} \varphi^{-1/3} \quad (31)$$

Where $I(A)$, $B(T)$ and $\rho_0(\text{kg}/\text{m}^3)$ represent the current intensity, the magnetic field value and the initial mass density of the injected gas respectively. The parameter φ is given by the formulae:

$$\varphi = \frac{1}{1+v_a} + v_a \quad (32)$$

v_a is the gas velocity close to the arc. This study is performed for electric arc current intensities in air at atmospheric pressure between 100 and 1760A in the presence of an external magnetic field for magnetic field intensities between 0.005 and 3.9T, covering the power range of the torch studied in this paper.

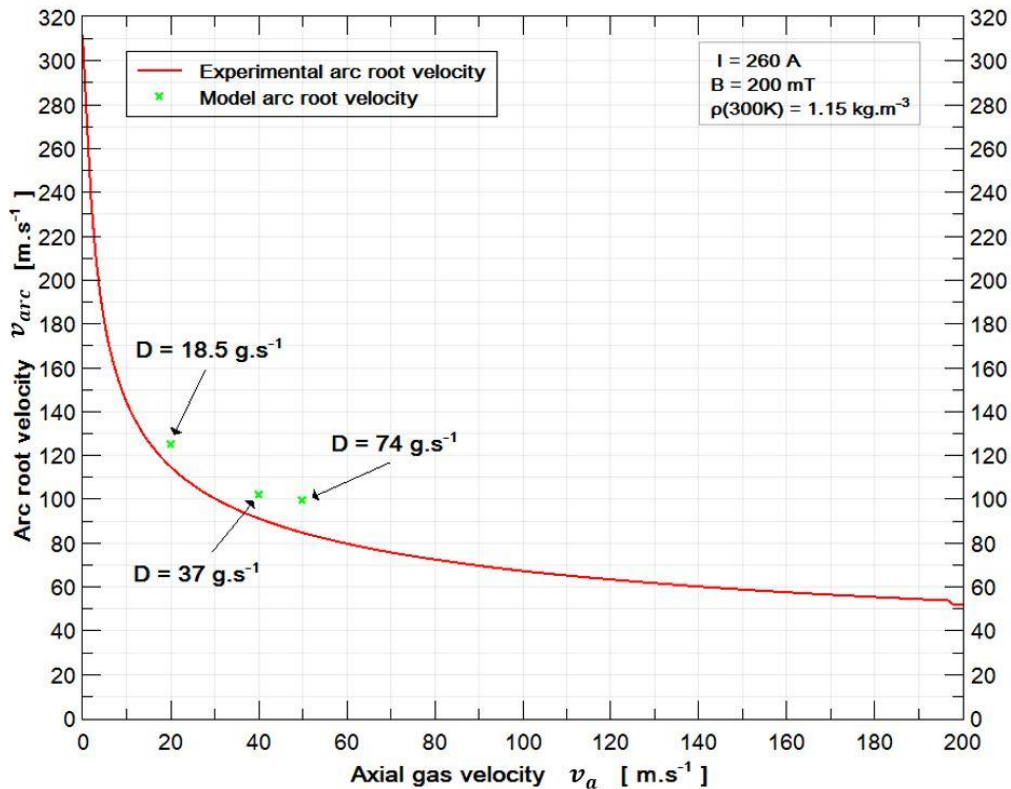


Figure 13 – rotational arc root velocity versus axial gas velocity

From the equations (31) and (32) given by Essiptchouk et al [32] it is possible to represent the rotational arc root velocity versus the axial gas velocity. Several quantities are necessary as the current intensity, the magnetic field, a mean mass density and the axial gas velocity. In order to draw the Figure 13, the current intensity is taken to $I = 260\text{A}$, the mass density as suggested by the author to its value at $T = 300\text{K}$ ($\rho_0 = 1.15 \text{ kg/m}^3$). An increase of the flow velocity leads to a decrease of the rotational velocity.

From the relation (31) of Essiptchouk et al, the axial velocity (v_a) is the most critical parameter to estimate. In their paper, the authors stipulate that the axial gas velocity is taken close to the arc but they haven't given any precision about its estimation. There for, in our model, we obtain for several values of inlet mass flow rate ($D = 18.5\text{g/s}$, $D = 37\text{g/s}$, $D = 74\text{g/s}$) the axial gas velocity near the arc (see column n°6 of the Table 2). For the external magnetic field value, we have taken its maximum value at the plasma area interaction, $B = 200\text{mT}$ (Figures 9 and 10). From the values of the axial gas velocity, the magnetic field, the current intensity and the mass density values, applying the equation (31), it is possible to estimate a theoretical arc root rotational velocity by our model. In Table 2 and Figure 13, we present the arc root rotational velocity value obtained experimentally by Essiptchouk et al [32] (see column n°7, in Table 2) and compared with the value founded by our model (last column in Table 2) estimated by relation (30).

Table 2 – Confrontation of arc root rotational velocity between experiment [32] and model

Case	$D(\text{g/s})$	$I(\text{A})$	$B(\text{Gauss})$	$\rho_0 (\text{kg/m}^3)$	v_a from the model	v_{arc} [28]	v_{arc} from the model
1	18.5	260	2000	1.15	20m/s	115 m/s	125 m/s
2	37	260	2000	1.15	40 m/s	91.32 m/s	102 m/s
3	74	260	2000	1.15	50 m/s	86 m/s	99.4 m/s

A good agreement is found between the rotational arc velocity found by the model and the formulation proposed by Essiptchouk. In this equation the torch dimensions as its radius are not explicit. Nevertheless, this dimension acts on the equation (32), greater is the cathode radius, smaller the gas velocity and the parameter φ are. Another study from S. Ghorui et al [5] has shown that the arc velocity obeys to the relationship:

$$v_{arc} \propto B^\gamma \quad (33)$$

In the literature the reported dependence of the γ coefficient varies from 0.34 to 0.60. In the case of an anode electrode and an arc current equals to 200A, with a magnetic field in reverse direction as us, the coefficient was found to $\gamma = 0.48$ [5]. In our study the same magnetic field value was applied for the three cases. Using $\gamma = 0.48$ and a value of the magnetic field equal to 200mT (2000 Gauss), the values of the arc velocities given in Table 2 lead from case 1 to 3 to proportionality coefficients respectively equal to 3.25, 2.65 and 2.58. For a given value of the magnetic field, the arc velocity increases with a diminution of the mass flow rate due to a decrease of the aerodynamic drag forces.

Nevertheless, it should be interesting as suggested by Brillhac et al [4] to study if a correlation exists between the convection in the hollow cathode considering cold gas and the complete plasma flow representation in presence of an electric arc. From the initial injected mass flow rate D , one part goes down directly in the anode direction and the other part goes up in the hollow cathode before descending on the axis. The axial position where the integrated mass flow rate is 30% reduced corresponds to the beginning position of the arc attachment position found by the model. The study was performed for an inlet mass flow rate of $D = 37 \text{ g/s}$ and verified for two other values $D = 18.5 \text{ g/s}$ and $D = 74 \text{ g/s}$ and a good agreement was found.

From these two empirics analysis the axial position and the rotational velocity can be deduced.

3.4. Plasma Characteristics

Based on the model developed, we present in this section general results on arc behavior. In the Figure 14, we present for different instants (10, 11 and 12ms), the temperature fields of the air plasma in middle plane ($x=0$) of

the torch. At the anode exit (Torch exit, see Figure 1) we present in the Figures 15 and 16, the fields and temperature profiles respectively for calculation instants, 10 to 15ms (step 1ms) in the two transverse directions (Ox) and (Oy). By observing the Figures 14, 15 and 16, we can notice that the fields and temperature profiles of the plasma show inhomogeneous distributions that evolve over time.

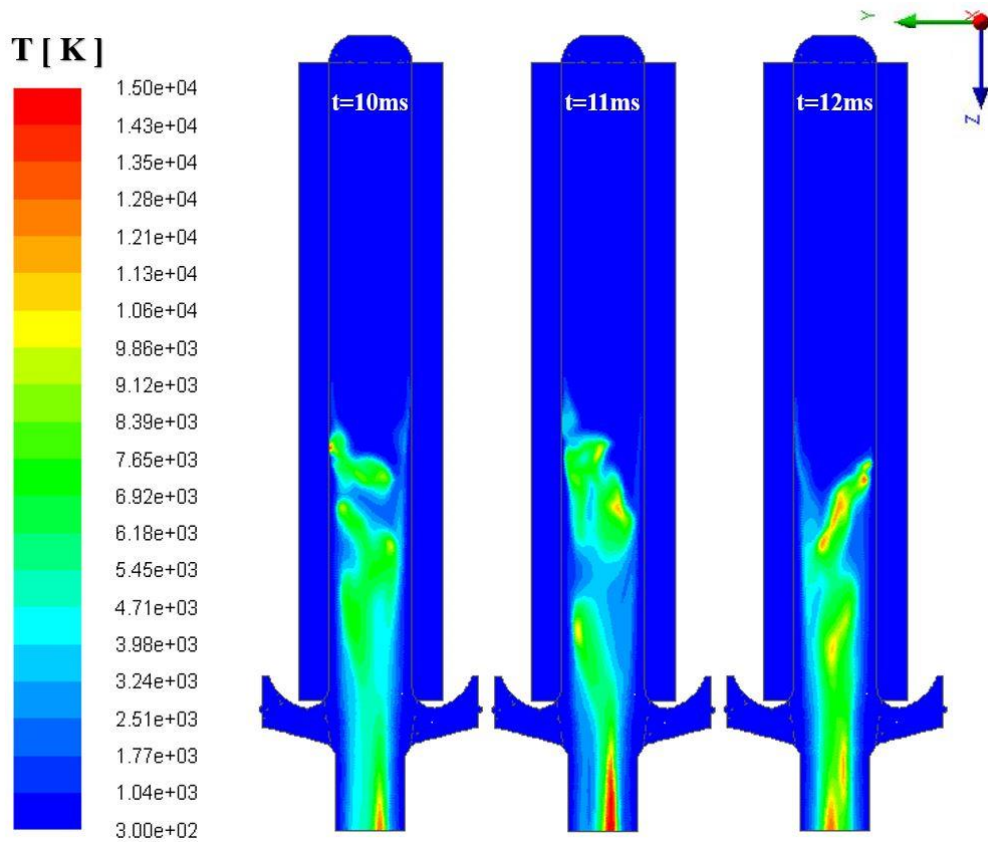


Figure 14 – Temperature fields in the hollow cathode (t=10, 11 and 12ms)

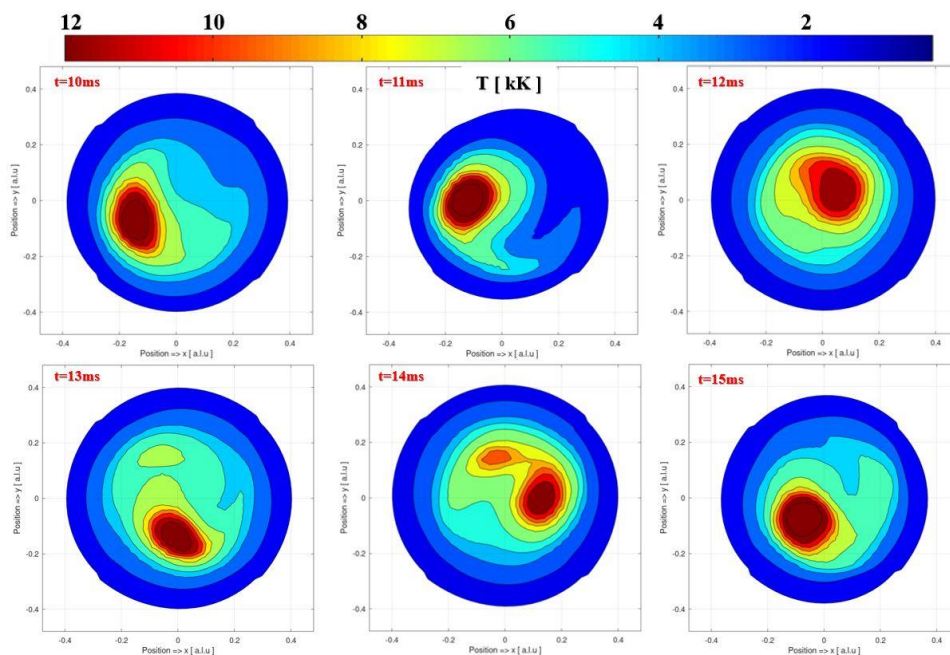


Figure 15 – Temperature fields at the exit plane from 10 to 15ms (step 1ms)

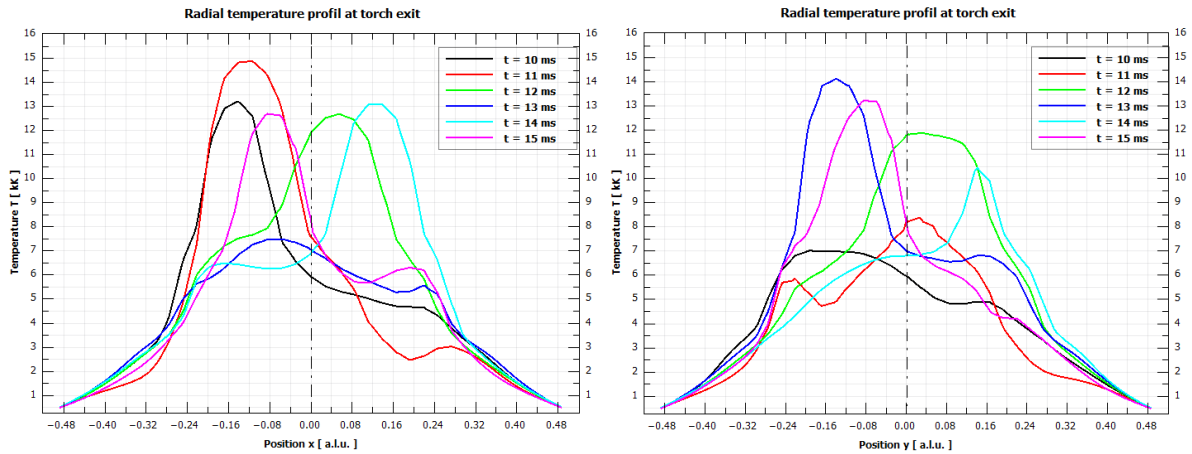


Figure 16 – Temperature profiles at the exit plane for different times on two perpendicular directions.

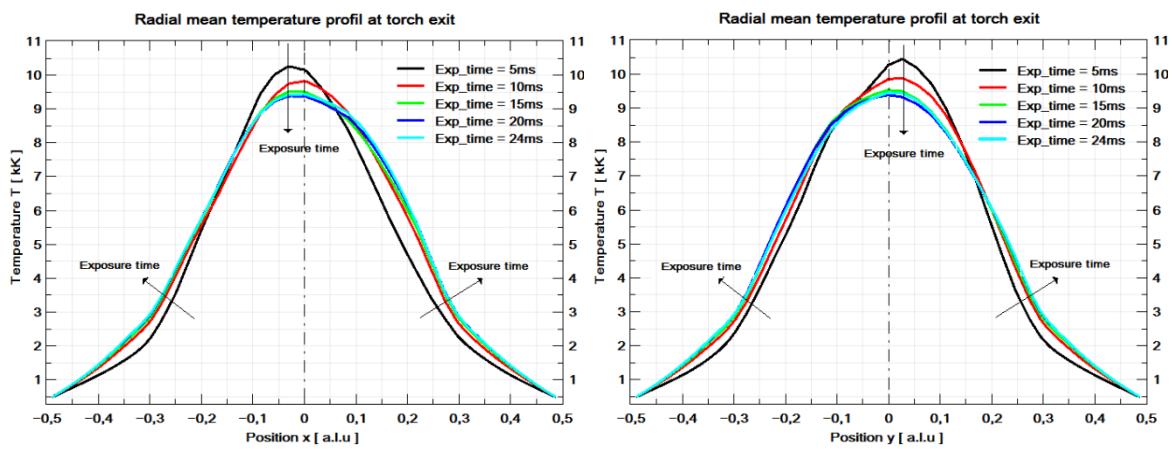


Figure 17 – Mean temperature profiles integrated on time at the exit plane for different integrated times on two perpendicular directions.

Figure 17 shows the average temperature profiles in the two transverse directions (Ox) and (Oy) on the output plane (Torch exit, Figure 1) for different values of the integration time of 5, 10, 15, 20 and 24ms. We can see in the Figure 17 that the mean temperature profiles tend towards a Gaussian-type mean temperature profile with the integrated time starting from an integrated time of 15ms. Note that such a Gaussian temperature profile could be imposed in initial boundary conditions for models interested in the study of the variations of the thermal characteristics in the anode and at the torch exit.

4. Conclusion

This work was related to the study of a hollow cathode torch whose arc root is rotated under the influence of an external magnetic field. In order to apprehend the plasma characteristics, a 3D temporal model is developed in the upstream part of the torch describing the injectors, the flow in the cathode and in a plane located at the anode inlet. The magneto hydrodynamic equations are solved using the Ansys Fluent code. The model developed takes into account the magnetic field generated by the external coil. Thus the magnetic field resulting at each point is the contribution of the external field and the magnetic field generated by the flow of current in the electric arc. In order to describe the movement and the arc attachment position an effective conductivity module has been implemented. It allows the new position of the arc root to be determined temporally and to include an additional voltage drop without having to finely describe the non-equilibrium sheaths at the arcing point.

The model highlights the tortuous nature of the arc under the influence of convective forces and the resulting magnetic field. It clearly shows the existence of unsymmetrical plasma at the entrance of the downstream electrode. However if the fields are integrated over 15ms a Gaussian profile is observed.

This tortuous character of the arc is also visible on the temporal variation of the tension. In relation to the parameters used, two characteristic times can be discerned: (1) the speed regulation time $t_1 = 3\text{ms}$, and (2) the stabilization time of the axial position, which is of the order of $t_2 = 26\text{ms}$.

Our model does not take into account the erosion of the electrodes due to the interaction of the arc during its attachment or under the effect of radiation. However, it allows us to determine the axial position of the arc root and its rotation speed. In order to compare this attachment position with experimental work, Europlasma has carried out ultrasonic measurements to determine the wear zones relative to the attachment of the rotating arc root. A good correlation was observed between the plasma interaction area determined by the model and the erosion zone. In case of a cold flow study the arc attachment area corresponds to the position where the upstream flow was 30% reduced.

The rotation frequency determined by the model is in the order of 1.14 kHz after stabilization. The theoretical rotation speed is in the order of 102m/s. This theoretical velocity was compared to the one calculated from a formula in the literature. A good agreement was found validating the results of our model.

The model thus allows to characterize the plasma in the upstream electrode and to determine the spatial and temporal positions of the arc hooking. We will now use this model to describe the downstream part of the torch.

Acknowledgement

The authors would like to thank the Europlasma Company for the ultrasonic measurements that were carried out.

References

- [1] Boulos M I, Fauchais P and Pfender E 1994 *Springer Science*, Fundamentals and applications, ISBN 978-1-4899-1337-1
- [2] Fauchais P and Vardelle A 2000 *Plasma Phys Control Fusion*, vol. 42, pp. B365–B383.
- [3] Laroche G 1991 *Book of Les plasmas dans l'industrie*, Electricité De France, ISBN 2-86995-017-9, 1991
- [4] Brilhac J F, Pateyron B, Coudert J F, Fauchais P and Bouvier A 1995 *Plasma Chemistry and Plasma Processing* vol. 15 no. 2
- [5] Ghorui S, Sahasrabudhe S N and Das A K 2010 *J. Phys. D: Appl. Phys.* **43** 245201 (18pp).
- [6] Ghorui S, Tiwari N, Meher K C, Jan A, Bhat A and Sahasrabudhe S N 2015 *Plasma Sources Sci. Technol.* **24** 065003 (10pp)
- [7] Hur M, Kim K S and Hong S H 2003 *Plasma Sources Sci. Technol.* **12** 255-264
- [8] Hur M and Hong S H 2002 *J. Phys. D: Appl. Phys.* **35** 1946-1954
- [9] Park J M, Kim K S, Hwang T H and Hong S H 2004 *IEEE Transactions on plasma science* vol. 32, no. 2
- [10] Mino H, Arsaoui A and Bouvier A 1995 *J. Phys. D: Appl. Phys.* **28** 1630-1648
- [11] Freton P, Gonzalez J J and Escalier G 2009 *J. Phys. D: Appl. Phys.* **42** 195205 (15pp).
- [12] Patankar S V 1980 *Book of Numerical Heat transfer and Fluid Flow*. ISBN 0891165223, Mc Graw Hill Compagny
- [13] Bacri J and Raffanel S 1989 *Plasma Chemistry and Plasma Processing* vol. 9, no.1
- [14] Sinkevich O A, Chikunov S E, Glazkov V V and Isaev E Kh 2002 Boundaries of stability of the plasma flow in cylindrical channels, TPP 7 Thermal Plasma Processes (Strasbourg, France) (Under press in the Progress in Plasma Processing of Materials 2002 published by Begell house, Inc, New York)
- [15] Naghizadeh-Kashani Y, Cressault Y and Gleizes A 2002 *J. Phys. D: Appl. Phys.* **35** 2925-2934
- [16] Freton P, Gonzalez J J, Masquère M and Reichert F 2011 *J. Phys. D: Appl. Phys.* **44** 345202 (16pp)
- [17] Lindmayer M, Marzahn E, Mutzke A, Rütther T and Springstube M 2006 *IEEE Trans. CPMT* vol. 29, no. 2, pp. 310-317
- [18] Karetta F and Lindmayer M 1998 *IEEE Trans. CPMT- 21 Part A*, 1998, pp. 96-103.
- [19] Karetta F 1998 *PhD Thesis* TU Braunschweig, Fortschritt-Bericht VDI Reihe 21, no. 250, VDI-Verlag, Duisseldorf
- [20] Lindmayer M, Springstube M 2001 *47th IEEE Holm Conference on Electrical Contacts*, Montreal, Canada
- [21] Lindmayer M, Springstube M 2001 *47th IEEE Holm Conference on Electrical Contacts*, Montreal, Canada
- [22] Ruimpler C, Reichert F, Stammberger H, Terhoeven P and Berger F 2006 *23rd International Conference on Electrical Contacts*, Sendai, Japan
- [23] Lindmayer M, Marzahn E, Mutzke A, Rütther T and Springstube M 2006 *IEEE Trans. CPMT*, vol. 29, no. 2, pp. 310-317
- [24] Rütther T, Mutzke A, Lindmayer M and Kurrat M 2006 *23rd International Conference on Electrical Contacts*, Sendai, Japan
- [25] Aaritz Ms I A 2013 *PhD Thesis* Modelization and Analysis of the Electric Arc in Low Voltage Circuit Breakers. Universidad Del Pais Vasco Euskal Herriko Unibertsitatea. url: <http://hdl.handle.net/10810/15849>

- [26] Mutzke A, Ruther T, Lindmayer M and Kurrat M 2008 24th *International Conference on Electrical Contacts*, St. Malo, France, 9-12 June
- [27] Benilov M S 2008 *J. Phys. D: Appl. Phys.* **41** 144001
- [28] Cayla F 2008 *PhD Thesis* Modélisation de l'interaction entre un arc électrique et une cathode. Université Toulouse III – Paul Sabatier, France
- [29] Conway J T 2001 *IEEE Transactions on Magnetics* Exact Solutions for the Magnetic Fields of Axisymmetric Solenoids and Current Distributions, vol. 37, no. 4
- [30] Abramovitz M and Stegun I S 1972 *Handbook of mathematical functions* (New York: Dover Publications) ISBN 0-486-61272-4
- [31] Mutzke A, Ruther T, Kurrat M, Lindmayer M, and Wilkening E D 2007 53rd *IEEE Holm Conf. on Electrical Contacts*, Pittsburgh, pp. 175-182
- [32] Essiptchouk A M, Sharakhovsky L I and Marotta A 2000 *J. Phys. D: Appl. Phys.* **33** 2591-2597